Main Manuscript for

Eccentricity-paced geomagnetic field and monsoon rainfall variations over the last 870 kyr

Weijian Zhou[a,b,c,1*], Xianghui Kong[a,b,1], Greig A. Paterson[d], Youbin Sun[a,e], Yubin Wu[b,f], Hong Ao[a], Feng Xian[a,b], Yajuan Du[a,b], Ling Tang[g], Jie Zhou[g], Zhengguo Shi[a], A. J. Timothy Jull[h,i], Guoqing Zhao[a,b], Zhisheng An[a,c*]

[a]State Key Laboratory of Loess, Institute of Earth Environment, Chinese Academy of Sciences, Xi'an 710061, China

[b]Shaanxi Key Laboratory of Accelerator Mass Spectrometry and Application, Xi'an AMS Center, Xi'an 710061, China

[c]Interdisciplinary Research Center of Earth Science Frontier, Beijing Normal University, Beijing 100875, China

[d]Geomagnetism Laboratory, Department of Earth, Ocean and Ecological Sciences, University of Liverpool, Liverpool, UK

[e]School of Human Settlements and Civil Engineering, Xi'an Jiaotong University, Xi'an 710049, China

[f]University of Chinese Academy of Sciences, Beijing 100049, China

[g]Xi'an Institute for Innovative Earth Environment Research, Xi'an 710061, China

[h]Isotope Climatology and Environmental Research Centre, Institute for Nuclear Research, Debrecen H-4026, Hungary

[i]University of Arizona, Tucson, Arizona 85721, USA

Contributed by Zhisheng An (anzs@loess.llqg.ac.cn)

* To whom correspondence should be addressed. **Email**: anzs@loess.llqg.ac.cn (Zhisheng An) and weijian@loess.llqg.ac.cn (Weijian Zhou)

[1]These authors contributed equally.

Author Contributions: Z.A. and W.Z. supervised the project. W.Z. designed the research and methods. W.Z. and X.K. wrote the original manuscript. W.Z., X.K. and F.X. collected and processed samples. X.K. and G.Z. performed experiments in the lab. W.Z. and X.K. performed the data analysis with help from G.A.P., Y.S., H.A., and Y.D. All authors participated in discussion and interpretation of the data and contributed to improving the manuscript.

Competing Interest Statement: The authors declare no competing interest.

Classification: Physical Sciences/Earth, Atmospheric, and Planetary Sciences

Keywords: Chinese loess; Cosmogenic ^{10}Be; Geomagnetic field; Asian monsoon rainfall; Orbital eccentricity

This PDF file includes:

Main Text

Figures 1 to 4

Abstract

Whether there are links between geomagnetic field and Earth's orbital parameters remains unclear. Synchronous reconstructions of parallel long-term quantitative geomagnetic field and climate change records are rare. Here, we present ^{10}Be-derived changes of both geomagnetic field and Asian monsoon (AM) rainfall over the last 870 kyr from the Xifeng loess-paleosol sequence on the central Chinese Loess Plateau. The $^{10}Be_{GM}$ flux (a proxy for geomagnetic field induced ^{10}Be production rate) reveals 13 consecutive geomagnetic excursions in the Brunhes chron, which are synchronized with the global records, providing key time markers for Chinese loess-paleosol sequences. The ^{10}Be-derived rainfall exhibits distinct ~100 kyr glacial-interglacial cycles, and superimposed precessional (~23 kyr) cycles that match with those in Chinese speleothem $\delta^{18}O$ record. We find that changes in the geomagnetic field and AM rainfall share a common ~100 kyr cyclicity, implying a likely eccentricity modulation of both the geomagnetic field and climate.

Significance Statement

Whether the geomagnetic field is forced by Earth's orbital parameters or related to climate has long been a controversial topic. Using Chinese loess ^{10}Be, we simultaneously derive a credible geomagnetic field record by removing the climate factors and a quantitative record of Asian monsoon (AM) rainfall for the past 870 kyr. We show that changes in ^{10}Be-derived geomagnetic field and AM rainfall contain a ~100 kyr cyclicity, indicating that both geomagnetic field and AM rainfall variability may be modulated by orbital eccentricity. We suggest that eccentricity influences AM rainfall through modulating the amplitude of precession, while eccentricity may affect the geomagnetic field through global ice volume changes.

Main Text

Introduction

Classical Milankovitch theory holds that the variation of Earth's orbital-induced summer solar insolation is the main driving force of global climate change (1). However, whether the geomagnetic field intensity is modulated by Earth's orbital parameters, or it interacts with paleoclimate change remains controversial (2). Previous studies reveal that Earth's orbital signals such as eccentricity and obliquity cycles have been observed in the records of paleomagnetic inclination/intensity from marine sediments (3–7), implying a likely relationship between geomagnetic field and orbital parameters. However, other studies have argued that sedimentary records of paleomagnetic intensity (relative paleointensity) may be contaminated by climate and/or sediment diagenetic processes (8–10), leaving the relationship between climate and the geomagnetic field inconclusive. This therefore leads to an apparent argument on the relationship between geomagnetic field, climatic change, and Earth's orbital parameters, with several hypotheses on the relationship between geomagnetic field intensity and Earth's climate (11–14). Synchronous orbital-scale reconstructions of both the climatic and geomagnetic signals from the same sedimentary sequence under the same time scale may enable a clearer understanding of any covariation of the geomagnetic field and climate related to Earth's orbital forcing.

The loess-paleosol sequence on the Chinese Loess Plateau provides continuous terrestrial records for both the geomagnetic field and Asian monsoon (AM) variations throughout the Quaternary (15–17). The long-lived cosmogenic nuclide ^{10}Be (~1.39 Ma half-life) from the loess-paleosol sequence is an ideal candidate for simultaneously disentangling the geomagnetic field and AM rainfall signals (18–20). The meteoric ^{10}Be is produced by cosmic-ray spallation in Earth's atmosphere and its production rate is governed by the geomagnetic field intensity, hence, its flux in sediments can be used to derive geomagnetic field records (21–24). Solar magnetic field variations can also influence atmospheric ^{10}Be production via fluctuations in solar wind rigidity (21), but it mainly acts on shorter periods than considered when exploring long-term geomagnetic field variation. Once produced in the atmosphere, ^{10}Be becomes attached to atmospheric dust particles at the surface and deposits on the ground mainly via scavenging during rainfall events (25). The ^{10}Be fallout flux to the ground thus can be deconvolved to quantitatively reconstruct the rainfall amount (26, 27). Once on the ground, ^{10}Be becomes an immobile oxidized component in eolian sediments, enabling robust extraction of both geomagnetic field and rainfall changes (18, 27).

The Xifeng loess section in the central Chinese Loess Plateau is located at mid-latitude where the production rate of meteoric ^{10}Be is very sensitive to changes of geomagnetic field intensity (28) and its deposition is closely associated with AM rainfall amount (18, 27). We have successfully reconstructed the history of paleomonsoon rainfall and geomagnetic field variations separately over the last 130 kyr and 550 kyr using loess ^{10}Be (19, 27), yet their potential relationship has not been investigated. Here we extend the paired reconstructions of geomagnetic intensity and monsoon rainfall back to 870 kyr to address their relationships under the same chronological framework.

Results and Discussion

Samples and Chronology. We collected Chinese loess samples from ~65 m thick loess-paleosol strata (S_0-S_8) at the Xifeng section by manually cutting freshly exposed hill slope profiles (*SI Appendix* and Fig. S1). We measured magnetic susceptibility, grain size, ^{10}Be concentration and bulk density for 1302 samples in laboratory (*SI Appendix*). The Chinese loess chronology has been established via interpolation between age control points using different models (17, 29, 30). Here, we constructed an initial grain-size age model by correlating changes of Xifeng loess grain size with the glacial-interglacial cycles in the marine isotope records (30, 31) (Fig. 1, Table S1). We then refined the initial timescale based on common features observed in the Xifeng ^{10}Be-based rainfall record and the absolute U/Th dated Chinese speleothem δ^{18}O variations (32) (Table S1). Reliability of the refined age model is further verified by good correlations between the time series of Xifeng loess ^{10}Be-derived geomagnetic reversal/excursions with those of two VADM stacks (33, 34) and ^{10}Be/^{9}Be stacks (23) from marine sediments (Fig. 2). Using this age model, the ^{10}Be concentrations have been corrected for radioactive decay and the loess accumulation rate is calculated to convert the ^{10}Be concentration into flux (*SI Appendix*).

^{10}Be-derived geomagnetic excursion events. The $^{10}Be_{GM}$ flux in Xifeng loess reflects the geomagnetic field modulated ^{10}Be production rate variation (Fig. 2, see Materials and Methods and *SI Appendix*). We also convert the $^{10}Be_{GM}$ flux into the absolute VADM for further comparison using a similar method reported in (23) (*SI Appendix* and Fig. S2). $^{10}Be_{GM}$ flux variation over the last 870 kyr matches well with the relative geomagnetic paleointensity stacks from SINT 2000 (33) and PISO 1500 (34) and with the ^{10}Be/^{9}Be ratio record from marine sediments (23). Geomagnetic polarity reversal/excursions are accompanied by abrupt drops of geomagnetic field intensity. Because ^{10}Be production rate is anti-correlated with geomagnetic field intensity (21), peaks of $^{10}Be_{GM}$ flux record in Xifeng loess can be used to detect globally recorded geomagnetic reversal/excursion events. In the $^{10}Be_{GM}$ flux record, the most prominent peak between ~770 and 786 kyr can be readily correlated to the Brunhes/Matuyama (B/M) geomagnetic polarity reversal (Fig. 2). The B/M reversal recorded in the paleosol layer S_7 is synchronous with those recorded in marine sediments and in ice cores (i.e., corresponding to MIS 19) (22, 23, 35), enabling a better correlation of Chinese loess with marine and ice-core records (20).

Another 13 $^{10}Be_{GM}$ flux peaks that exceed more than 30% amplitude of the relative loess $^{10}Be_{GM}$ flux variation at B/M reversal (at least higher than long-term average $^{10}Be_{GM}$ flux value +0.5σ) are identified (Fig. 2A). By correlating these $^{10}Be_{GM}$ flux peaks with global geomagnetic records, 13 successive geomagnetic excursions in the Brunhes chron were identified, including Laschamp (~43 kyr), Norwegian Greenland Sea (~66 kyr), Fram Strait (~93 kyr), Blake (~120 kyr), Baffin Bay/6α (~163 kyr), Iceland Basin (~188 kyr), Pringle Falls (~205 kyr), Portuguese Margin (~284 kyr), Levantine (~373 kyr), Emperor (~472 kyr), Big Lost (~540 kyr), La Palma/15β (~593 kyr), and Stage 17/Osaka Bay (~674 kyr) (Fig. 2) (23, 36–41). Moreover, a significant $^{10}Be_{GM}$ flux peak at ~440 kyr is correlated with the troughs in SINT 2000 and PISO 1500 stacks and the marine $^{10}Be/^{9}Be$ ratio peaks of similar age, although there is no reported excursion that can be assigned to this record. Another possible excursion, West Eifel 1, may be assigned to the $^{10}Be_{GM}$ flux peak at ~730 kyr (42) although it does not reach our 0.5σ threshold. It appears that most of the geomagnetic polarity events tended to occur in the interglacial, interstadial stages, or the transition of interglacial/glacial as shown by correlating with loess grain size and benthic δ^{18}O records (Fig. 2A, E and F).

The $^{10}Be_{GM}$ flux record from Xifeng loess provides the first long and continuous geomagnetic record from terrestrial sediments over the past 870 kyr, with coverage of globally reported geomagnetic excursions during Brunhes chron and the B/M reversal. The good agreement between ^{10}Be-derived geomagnetic reversal/excursions and those from around the globe (Fig. 2) confirms that Chinese loess is qualified to record the global geomagnetic field variations, supporting that our chronology is robust. More importantly, these geomagnetic events provide independent time markers for correlating Chinese loess-paleosol sequences with global records (e.g., marine sediments and ice cores).

^{10}Be-derived AM rainfall variability. The ^{10}Be-derived AM rainfall from Xifeng loess ranges from ~300 mm/yr in glacials to ~1000 mm/yr in interglacials over the last 870 kyr (Fig. 3D, *SI Appendix*). Glacial-interglacial (~100 kyr) cycles are prominent in the ^{10}Be-estimated rainfall, which correlates with the global ice volume change as indicated by the benthic δ^{18}O record (31) (Fig. 3E). In addition to the ~100 kyr cycle, precession cycles in the ^{10}Be-rainfall record are in good agreement with variations of the 640 kyr Chinese speleothem δ^{18}O records (32) (Fig. 3B). The ~100 kyr cyclicity in ^{10}Be-derived AM rainfall may be related to its relatively high mid-latitude (~36°N) in the north of Qinling mountains whereas the ~23 kyr speleothem record (~32°N) in the south of Qinling mountains (Fig. S1A). With an average altitude of about 2500 m, the Qinling mountains have an important influence on atmospheric circulation in the troposphere, and serve as a key boundary dividing the northern and southern climates in China and the East Asian Continent (43). The AM climate variations recorded by speleothem (south of Qinling mountains) and loess deposits (north of Qinling mountains) are both affected by the low-latitude monsoon circulation (18, 27, 32, 44). The AM climate recorded by loess in north of the Qinling mountains, however, also responds sensitively to high-latitude and inland cold air circulation relevant to ice volume changes (45, 46).

A high-pass (<23 kyr) filtered results of the ^{10}Be-derived rainfall and speleothem $\delta^{18}O$ records show cycle-to-cycle correlation (Fig. 3C), except for attenuated correlation between ~500 kyr to ~640 kyr corresponding to S_5, which is a paleosol affected by prolonged and enhanced pedogenesis. The ^{10}Be-estimated rainfall amount during S_5 is comparable to that of other paleosol interglacials, differing from the remarkable increase of magnetic susceptibility at S_{5-1} (MIS 13) (Fig. 1). While magnetic susceptibility indicates that the summer monsoon intensity is extremely high during MIS 13, many proxies such as speleothem $\delta^{18}O$, Chinese loess $\delta^{13}C$ and δD_{wax} records exhibit similar summer monsoon intensity during all the past interglacials since 870 kyr (32, 47, 48). These proxy discrepancies demonstrate that monsoon rainfall amount is not always equivalent to the summer monsoon intensity. Moreover, the S_5 (MIS 13-15) interglacial is characterized by prolonged high monsoon rainfall, with relatively weaker precessional fluctuations than shown in other interglacials (Fig. 3D). These special features may be caused by a strong asymmetry of hemispheric climates during MIS 13 (49, 50) and the extra-long interglaciation in NH during MIS 13-15 (51), which lead to atypical pedogenic processes in S_5. The long duration of pedogenesis would have promoted magnetic susceptibility enhancement, but might attenuate the sensitivity of AM rainfall response to precession-induced insolation variation.

Based on the ^{10}Be-rainfall record, we also find that the amplitude of the precession signal in AM rainfall is highly related to eccentricity variability. The 23 kyr (±20%) bandpass filtered from ^{10}Be-rainfall curve matches well with Earth's precession variation both in terms of frequency and amplitude (Fig. S3). The amplitude of the precession cycle in the ^{10}Be-rainfall was reduced during ~300-600 kyr and enhanced significantly around ~100-300 kyr and ~600-700 kyr. The only exception is reduced precessional rainfall variability during S_5 or MIS13-15 with high eccentricity.

Dynamically, eccentricity could influence AM rainfall through two mechanisms, one is its direct modulation of precession amplitude (52, 53) and the other is an indirect effect through global ice volume changes (54). The classical sea-breeze monsoon mechanism involves increased low-latitude boreal summer insolation leading to surface warming and amplified land/sea temperature contrast, in turn, enhancing atmospheric water content, low-level advective convergence and thus rainfall over land (55, 56). Eccentricity-modulated low-latitude interhemispheric insolation gradient also contributes to the precessional amplitude variability of monsoon rainfall (Fig. 3A, Fig. S3), since increased insolation difference between the northern and southern hemispheres can result in more intense cross-equatorial pressure gradient and monsoon circulation (18, 27, 57–59). Indirectly, eccentricity-induced amplitude modulation of summer insolation can generate large-amplitude glacial cycles (54). Strong northern hemispheric cooling by large ice sheets leads to decreased local land-sea thermal contrast, high-tropospheric westerly wave train and significant feedback of dust aerosols, thus weakening the East Asian summer rainfall during glaciations (60). We suggest that both direct and indirect mechanisms are responsible for the apparently warmer/wetter interglacial periods and larger precessional climate oscillations observed during periods of increased variance of eccentricity.

Co-variation of geomagnetic field and monsoon climate on eccentricity timescales. There is a consensus that the geomagnetic field protects Earth's life and environment from cosmic-ray radiation by shielding the surface from high-energy particles (13). However, there are still different views on whether there is correlation between geomagnetic field intensity and Earth's climate (61–63). Our ^{10}Be-reconstructed geomagnetic field ($^{10}Be_{GM}$ flux) and AM rainfall variations over the past 870 kyr make it possible to explore the relationship between geomagnetic field and orbital forcing. Comparison between the ^{10}Be-rainfall and the $^{10}Be_{GM}$ flux shows that increased monsoon rainfall generally corresponds to the decreased geomagnetic field intensity ($^{10}Be_{GM}$ flux increases) (Fig. 4A). Meanwhile, the geomagnetic reversal/excursions occurred mainly in the interglacial, interstadial stages, or the transition of interglacial/glacial (Fig. 2). The spectral results show that AM rainfall is dominated by orbital cycles at both ~100 kyr and ~23 kyr periods, while the $^{10}Be_{GM}$ flux only shows a 100 kyr cyclicity (Fig. 4B). The ~100 kyr periodicity of geomagnetic field change is also evident in global relative geomagnetic paleointensity records, including a $^{10}Be/^{9}Be$ ratio stack, and two VADM stacks from marine sediments (Fig. S4) (23, 33, 34).

A cross-wavelet spectrum between the AM rainfall and $^{10}Be_{GM}$ flux time series exhibits a strong coherency at ~100 kyr period (Fig. 4C). We infer that the common ~100 kyr periodic variations of the geomagnetic field and AM rainfall are likely related to the modulation by orbital eccentricity variability. Eccentricity modulates the ~100 kyr glacial cycle and precessional amplitude variations of AM rainfall. As for geomagnetic field, the main geomagnetic field is generated by movement of liquid iron in Earth's outer core, a process known as the geodynamo (64, 65). Thermochemical convection is the main power source in the core, but changes of Earth's motion state play a role in controlling the patterns of convection, hence, the generation of the geomagnetic field (65, 66). Earth's eccentricity-paced ~100 kyr glacial cycles (54) lead to redistribution of global water between global oceans and polar ice sheets (61, 67). During glacial periods, a relative increase of mass distributed at high latitude can lead to an increase in Earth's rotational velocity through conservations of angular momentum (11, 68, 69) (Fig. S6) and therefore a decrease of length of day (LOD). LOD correspondingly increases as these ice caps recede redistributing mass away from the poles. Decadal to millennial scale variations in Earth's rotation rate (or LOD) are suggested to be linked to geomagnetic secular variation and geodynamo simulations suggest that small periodic changes in LOD can manifest as amplified variations in dipole field strength with a similar period (64, 66). We speculate that the shifting glacial mass distribution over the eccentricity-paced glacial-interglacial cycles may have a sufficiently large impact on Earth's rotation rate to manifest as a ~100 kyr signal in the geomagnetic field strength (11, 61). This is consistent with the common ~100 kyr cyclicity in the cross-wavelet analysis between benthic $\delta^{18}O$ and $^{10}Be_{GM}$ flux (Fig. S7). Finally, the cross-wavelet analysis between ^{10}Be-rainfall and $^{10}Be_{GM}$ flux indicates that their variations are in-phase before ~550 kyr, but 90° out of phase since ~400 kyr (Fig. 4C, the arrows vary through time), indicating a complex or unstable responses of AM rainfall and geomagnetic field intensity to Earth's eccentricity variations. Such phase changes may be partly related to different orbital cycles (~100 kyr and ~23 kyr for ^{10}Be-rainfall and ~100 kyr for $^{10}Be_{GM}$ flux). Future studies are needed to confirm the above interpretation of a possible link between Earth's orbital eccentricity and geomagnetic field variations.

To summarize, we reconstruct the relative geomagnetic field intensity and AM rainfall records from Chinese loess ^{10}Be over the last 870 kyr. Based on the ^{10}Be-derived geomagnetic field intensity variations, successive global geomagnetic excursions have been identified for the first time in a Chinese loess-paleosol sequence. The quantitative reconstruction of AM rainfall shows both ~100 kyr glacial-interglacial and ~23 kyr cycles, while the ^{10}Be-derived geomagnetic field variation has a predominant ~100 kyr cyclicity. Our geomagnetic field and AM rainfall records provide reliable evidence that eccentricity likely modulates both the geomagnetic field and climate, resulting in their co-variation on orbital time scales. This is likely due to eccentricity-induced mass transfer through the formation and melting of polar ice-caps, impacting Earth's rotation rate and thus the geomagnetic field.

Materials and Methods

^{10}Be Sample Preparation. Approximately 1 g of loess sample was spiked with ~0.5 mg ^{9}Be carrier and leached in HCl along with H_2O_2 over night to remove calcium carbonate and organic matter. The sample solution was centrifuged, the supernatant was collected and dried into salts which were then dissolved in HCl. The Be in this dissolved solution was separated on cation-exchange resin columns in 1 M HCl, then precipitated as hydroxides, and transformed to oxides (BeO) in a muffle furnace at 900 °C. BeO was mixed with copper powder for $^{10}Be/^{9}Be$ measurement by 3MV Accelerator Mass Spectrometer at Xi'an AMS Center, Institute of Earth Environment, Chinese Academy of Sciences (*SI Appendix*).

Reconstructions of geomagnetic field and AM rainfall from loess ^{10}Be. The loess ^{10}Be variation was controlled by both the climate factors and geomagnetic field intensity modulation. The climate components in the loess ^{10}Be came from long-range dust input from the source regions and the in-situ atmospheric fallout by wet precipitation (18). Similarly, loess magnetic susceptibility (χ) also contains the detrital fraction from the primary eolian dust and a pedogenic fraction formed during post-depositional soil development. Therefore, loess χ and ^{10}Be concentration were strongly correlated (*SI Appendix*). By using a detrital end-number of loess χ (i.e., SUS(D)) to estimate the dust fraction of ^{10}Be (i.e., ^{10}Be(D)) (*SI Appendix* and Fig. S5), we can differentiate the pedogenic fraction of χ (i.e., SUS(P)) and the ^{10}Be components only associated with wet precipitation rate and geomagnetic field intensity (i.e., ^{10}Be(P, GM)). The linear regression between SUS(P) and ^{10}Be(P, GM) allows us to further remove the precipitation effect from ^{10}Be(P, GM) (*SI Appendix*). After removing the detrital and pedogenic contributions, the residual ^{10}Be flux (i.e., $^{10}Be_{GM}$ flux) reflects primarily the meteoric ^{10}Be production rate variation modulated by geomagnetic field changes, which is supported by similar variability to the SINT 2000 (33) and PISO 1500 VADM stacks (34), as well as $^{10}Be/^{9}Be$ ratio stack from marine sediments (23) (Fig. 2). By correcting the ^{10}Be(P, GM) flux for variations in ^{10}Be production rate linked to changes in magnetic field intensity (27), a

^{10}Be(P) flux only dependent on wet precipitation was obtained and used to calculate AM rainfall (*SI Appendix*).

References

1. M. Milankovitch, Canon of insolation and the ice-age problem (Kanon der Erdbestrahlung und seine Anwendung auf das E iszeitenproblem) Belgrade, 1941.
2. N. A. Kilifarska, V. G. Bakhmutov, G. V Melnyk, "Chapter 2 - Variations and covariation in palaeoclimate and palaeomagnetic field" in N. A. Kilifarska, V. G. Bakhmutov, G. V. B. T.-T. H. L. between E. M. F. and C. Melnyk, Eds. (Elsevier, 2020), pp. 25–42.
3. T. Yamazaki, N. Ioka, Long-term secular variation of the geomagnetic field during the last 200 kyr recorded in sediment cores from the western equatorial Pacific. *Earth Planet. Sci. Lett.* **128**, 527–544 (1994).
4. J. E. T. Channell, D. A. Hodell, J. McManus, B. Lehman, Orbital modulation of the Earth's magnetic field intensity. *Nature* **394**, 464–468 (1998).
5. T. Yamazaki, H. Oda, Orbital influence on Earth's magnetic field: 100,000-Year periodicity in inclination. *Science* **295**, 2435–2438 (2002).
6. Y. Yokoyama, T. Yamazaki, H. Oda, Geomagnetic 100-kyr variation excited by a change in the Earth's orbital eccentricity. *Geophys. Res. Lett.* **37** (2010).
7. G. Wollin, W. B. F. Ryan, D. B. Ericson, J. H. Foster, Paleoclimate, paleomagnetism and the eccentricity of the Earth's orbit. *Geophys. Res. Lett.* **4**, 267–270 (1977).
8. D. V. Kent, Apparent correlation of palaeomagnetic intensity and climatic records in deep-sea sediments. *Nature* **299**, 538–539 (1982).

9. Y. Guyodo, P. Gaillot, J. E. T. Channell, Wavelet analysis of relative geomagnetic paleointensity at ODP Site 983. *Earth Planet. Sci. Lett.* **184**, 109–123 (2000).

10. C. Xuan, J. E. T. Channell, Testing the relationship between timing of geomagnetic reversals/excursions and phase of orbital cycles using circular statistics and Monte Carlo simulations. *Earth Planet. Sci. Lett.* **268**, 245–254 (2008).

11. H. U. Worm, A link between geomagnetic reversals and events and glaciations. *Earth Planet. Sci. Lett.* **147**, 55–67 (1997).

12. K. S. Carslaw, R. G. Harrison, J. Kirkby, Cosmic Rays, Clouds, and Climate. *Science* **298**, 1732–1737 (2002).

13. A. Cooper, *et al.*, A global environmental crisis 42,000 years ago. *Science* **371**, 811–818 (2021).

14. M. F. Knudsen, P. Riisager, Is there a link between Earth's magnetic field and low-latitude precipitation? *Geology* **37**, 71–74 (2009).

15. F. Heller, T. Liu, Magnetostratigraphical dating of loess deposits in China. *Nature* **300**, 431–433 (1982).

16. Z. An, *et al.*, The long-term paleomonsoon variation recorded by the loess-paleosol sequence in central China. *Quat. Int.* **7**, 91–95 (1990).

17. Y. Sun, S. C. Clemens, Z. An, Z. Yu, Astronomical timescale and palaeoclimatic implication of stacked 3.6 Myr monsoon records from the Chinese Loess Plateau. *Quat. Sci. Rev.* **25**, 33–48 (2006).

18. W. Zhou, *et al.*, Disentangling geomagnetic and precipitation signals in an 80-kyr Chinese loess record of ^{10}Be. *Radiocarbon* **49**, 139–160 (2007).

19. W. Zhou, *et al.*, Reconstruction of 130-kyr relative geomagnetic intensities from ^{10}Be in two Chinese loess sections. *Radiocarbon* **52**, 129–147 (2010).

20. W. Zhou, *et al.*, Timing of the Brunhes-Matuyama magnetic polarity reversal in Chinese loess using ^{10}Be. *Geology* **42**, 467–470 (2014).

21. J. Masarik, J. Beer, Simulation of particle fluxes and cosmogenic nuclide production in the Earth's atmosphere. *J. Geophys. Res.* **104**, 12099–12111 (1999).

22. G. M. Raisbeck, F. Yiou, O. Cattani, J. Jouzel, ^{10}Be evidence for the Matuyama-Brunhes geomagnetic reversal in the EPICA Dome C ice core. *Nature* **444**, 82–84 (2006).

23. Q. Simon, *et al.*, Authigenic ^{10}Be/^{9}Be ratio signatures of the cosmogenic nuclide production linked to geomagnetic dipole moment variation since the Brunhes/Matuyama boundary. *J. Geophys. Res. Solid Earth* **121**, 7716–7741 (2016).

24. M. Zheng, et al., Geomagnetic dipole moment variations for the last glacial period inferred from cosmogenic radionuclides in Greenland ice cores via disentangling the climate and production signals. *Quat. Sci. Rev.* **258** (2021).

25. A. M. Smith, et al., ^{7}Be and ^{10}Be concentrations in recent firn and ice at Law Dome, Antarctica. *Nucl. Instruments Methods Phys. Res. Sect. B Beam Interact. with Mater. Atoms* **172**, 847–855 (2000).

26. W. Zhou, F. Xian, Y. Du, X. Kong, Z. Wu, The last 130 ka precipitation reconstruction from Chinese loess ^{10}Be. *J. Geophys. Res. Solid Earth* **119**, 2013JB010296 (2014).

27. J. W. Beck, *et al.*, A 550,000-year record of East Asian monsoon rainfall from ^{10}Be in loess. *Science* **360**, 877–881 (2018).

28. G. Wagner, *et al.*, Reconstruction of the geomagnetic field between 20 and 60 kyr BP from cosmogenic radionuclides in the GRIP ice core. *Nucl. Instruments Methods Phys. Res. Sect. B Beam Interact. with Mater. Atoms* **172**, 597–604 (2000).

29. G. Kukla, *et al.*, Pleistocene climates in China dated by magnetic susceptibility. *Geology* **16**, 811–814 (1988).

30. S. C. Porter, Z. An, Correlation between climate events in the North Atlantic and China during the last glaciation. *Nature* **375**, 305–308 (1995).

31. L. E. Lisiecki, M. E. Raymo, A Pliocene-Pleistocene stack of 57 globally distributed benthic $\delta^{18}O$ records. *Paleoceanography* **20**, 1–17 (2005).

32. H. Cheng, *et al.*, The Asian monsoon over the past 640,000 years and ice age terminations. *Nature* **534**, 640–646 (2016).

33. J. P. Valet, L. Meynadier, Y. Guyodo, Geomagnetic dipole strength and reversal rate over the past two million years. *Nature* **435**, 802–805 (2005).

34. J. E. T. Channell, C. Xuan, D. A. Hodell, Stacking paleointensity and oxygen isotope data for the last 1.5 Myr (PISO-1500). *Earth Planet. Sci. Lett.* **283**, 14–23 (2009).

35. Q. Simon, *et al.*, Increased production of cosmogenic ^{10}Be recorded in oceanic sediment sequences: Information on the age, duration, and amplitude of the geomagnetic dipole moment minimum over the Matuyama–Brunhes transition. *Earth Planet. Sci. Lett.* **489**, 191–202 (2018).

36. S. Lund, J. S. Stoner, J. E. T. T. Channell, G. Acton, A summary of Brunhes paleomagnetic field variability recorded in Ocean Drilling Program cores. *Phys. Earth Planet. Inter.* **156**, 194–204 (2006).

37. C. G. Langereis, M. J. Dekkers, L. G. J. De, M. Paterne, S. P. J. M. Van, Magnetostratigraphy and astronomical calibration of the last 1.1 Myr from an eastern Mediterranean piston core and dating of short events in the Brunhes. *Geophys. J. Int.*, 75–94 (1997).

38. C. Laj, J. E. T. Channell, "Geomagnetic Excursions" in *Treatise on Geophysics (Second Edition)*, G. Schubert, Ed. (Elsevier, 2015), pp. 343–383.

39. G. M. Raisbeck, *et al.*, An improved north-south synchronization of ice core records around the 41 kyr ^{10}Be peak. *Clim. Past* **13**, 217–229 (2017).

40. J. E. T. Channell, B. S. Singer, B. R. Jicha, Timing of Quaternary geomagnetic reversals and excursions in volcanic and sedimentary archives. *Quat. Sci. Rev.* **228**, 106114 (2020).

41. Q. Simon, N. Thouveny, D. L. Bourlès, J. P. Valet, F. Bassinot, Cosmogenic ^{10}Be production records reveal dynamics of geomagnetic dipole moment (GDM) over the Laschamp excursion (20–60 ka). *Earth Planet. Sci. Lett.* **550**, 116547 (2020).

42. B. S. Singer, K. A. Hoffman, E. Schnepp, Hervé Guillou, Multiple Brunhes Chron excursions recorded in the West Eifel(Germany) vocanics: Support for long-held mantle control over the non-axial dipole field. *Phys. Earth Planet. Inter.*, 28–40 (2008).

43. Y. Dong, et al., Co-evolution of the Cenozoic tectonics, geomorphology, environment and ecosystem in the Qinling Mountains and adjacent areas, Central China. *Geosystems and Geoenvironment* **1**, 100032 (2022).

44. Y. Wang, et al., Millennial- and orbital-scale changes in the East Asian monsoon over the past 224,000 years. *Nature* **451**, 1090–1093 (2008).

45. H. Ao, et al., Different orbital rhythms in the Asian summer monsoon records from North and South China during the Pleistocene. *Glob. Planet. Change* **80–81**, 51–60 (2012).

46. Y. Sun, et al., Astronomical and glacial forcing of East Asian summer monsoon variability. *Quat. Sci. Rev.* **115**, 132–142 (2015).

47. Y. Sun, *et al.*, Diverse manifestations of the mid-Pleistocene climate transition. *Nat Commun* **10**, 352 (2019).

48. Z. Wang, *et al.*, New chronology of the Chinese loess-paleosol sequence by leaf wax δD records during the past 800 k.y. *Geology* **49**, 847–850 (2021).

49. Q. Yin, *et al.*, The Eurasian ice sheet reinforces the East Asian summer monsoon during the interglacial 500 000 years ago. *Clim. Past* **4**, 79–90 (2008).

50. Z. Guo, A. Berger, Q. Yin, L. Qin, Strong asymmetry of hemispheric climates during MIS-13 inferred from correlating China loess and Antarctica ice records. *Clim. Past* **5**, 21–31 (2009).

51. Q. Hao, L. Wang, F. Oldfield, Z. Guo, Extra-long interglacial in Northern Hemisphere during MISs 15-13 arising from limited extent of Arctic ice sheets in glacial MIS 14. *Sci. Rep.* **5** (2015).

52. A. Berger, M. F. Loutre, Insolation values for the climate of the last 10 million years. *Quat. Sci. Rev.* **10**, 297–317 (1991).

53. X. Liu, Z. Shi, Effect of precession on the Asian summer monsoon evolution: A systematic review. *Chinese Sci. Bull.* **54**, 3720–3730 (2009).

54. A. Abe-Ouchi, *et al.*, Insolation-driven 100,000-year glacial cycles and hysteresis of ice-sheet volume. *Nature* **500**, 190–193 (2013).

55. J. E. Kutzbach, P. J. Guetter, The influence of changing orbital parameters and surface boundary conditions on climate simulations for the past 18 000 years. *J. Atmos. Sci.* **43**, 1726–1759 (1986).

56. T. M. Merlis, T. Schneider, S. Bordoni, I. Eisenman, The tropical precipitation response to orbital precession. *J. Clim.* **26**, 2010–2021 (2013).

57. D. C. Leuschner, F. Sirocko, Orbital insolation forcing of the Indian Monsoon – a motor for global climate changes? *Palaeogeogr. Palaeoclimatol. Palaeoecol.* **197**, 83–95 (2003).

58. Z. An, *et al.*, Glacial-interglacial Indian summer monsoon dynamics. *Science* **333**, 719–723 (2011).

59. B. A. Maher, Palaeoclimatic records of the loess/palaeosol sequences of the Chinese Loess Plateau. *Quat. Sci. Rev.* **154**, 23–84 (2016).

60. Z. Shi, *et al.*, Radiative effect of mineral dust on East Asian summer monsoon during the Last Glacial Maximum: Role of snow - albedo feedback. *Geophys. Res. Lett.* **46**, 10901–10909 (2019).

61. M. R. Rampino, Possible relationships between changes in global ice volume, geomagnetic excursions, and the eccentricity of the Earth's orbit. *Geology* **7**, 584–587 (1979).

62. V. Courtillot, Y. Gallet, J.-L. Le Mouël, F. Fluteau, A. Genevey, Are there connections between the Earth's magnetic field and climate? *Earth Planet. Sci. Lett.* **253**, 328–339 (2007).

63. L. Tauxe, T. Yamazaki, "Paleointensities" in *Treatise on Geophysics (Second Edition)*, Second Edi, G. Schubert, Ed. (Elsevier, 2015), pp. 461–509.

64. M. Dumberry, J. Bloxham, Azimuthal flows in the Earth's core and changes in length of day at millennial timescales. *Geophys. J. R. Astron. Soc.* **165**, 32–46 (2006).
65. C. Jones, "Geodynamo" in *Encyclopedia of Geomagnetism and Paleomagnetism*, D. Gubbins, E. Herrero-Bervera, Eds. (Springer Netherlands, 2007), pp. 287–296.
66. T. Miyagoshi, Y. Hamano, Magnetic field variation caused by rotational speed change in a magnetohydrodynamic dynamo. *Phys. Rev. Lett.* **111**, 124501 (2013).
67. W. F. Ruddiman, "The last Glacial maximum" in Earth's Climate: past and future, (W. H. Freeman and Company, 2001), pp. 253-272.
68. C. S. M. Doake, A possible effect of ice ages on the Earth's magnetic field. *Nature* **267**, 415–417 (1977).
69. J. X. Mitrovica, et al., Reconciling past changes in Earth's rotation with 20th century global sea-level rise: Resolving Munk's enigma. *Sci. Adv.* **1**, e1500679 (2015).

Acknowledgments

We are grateful to the valuable discussions about the manuscript with Dr. J.W. Beck. We also thank Mr. M. Liu, W.P. Li and Ms. C.W. Pan for part of loess ^{10}Be sample preparation. This work is jointly supported by grants from the Chinese Academy of Sciences (Nos. XDB40010100 and QYZDY-SSW-DQC010), the National Natural Science Foundation of China (No. 41930321), the Fund of Shandong Province (No. LSKJ202203300), the Ministry of Science and Technology of China (No. 2019YFC1509100), the International Partnership Program of Chinese Academy of Sciences (No. 132B61KYSB20170005), the Open-end Fund Program of State Key Laboratory of Loess and Quaternary Geology, Institute of Earth Environment, Chinese Academy of Sciences (SKLLQGZD1601), and the

Shaanxi Provence Youth Talent Support Program. G.A.P. is supported by a Natural Environment Research Council (NERC) Independent Research Fellowship (NE/P017266/1). A.J.T.J acknowledges partial support from the European Union and the State of Hungary, co-financed by the European Regional Development Fund in the project of GINOP-2.3.2-15-2016-00009 'ICER'.

Figures

Figure 1. Comparison of Xifeng loess proxies with benthic δ^{18}O stack. (A-C) Xifeng loess ^{10}Be concentration, mean grain size (MGS), and magnetic susceptibility (χ) on depth scale. (D) LR04 benthic δ^{18}O stack (31). The grey bars denote interglacial stages (MIS 1–21). L and S indicate the Chinese loess and paleosol layers. The numbers on the bottom indicate interglacial marine isotope stages 1-21.

Figure 2. Comparison of loess ^{10}Be derived paleomagnetic polarity events with marine geomagnetic paleointensity records. (A) Standardized geomagnetic modulated ^{10}Be flux derived from Xifeng loess (gray) and 5 points averaging curve (blue). (B) SINT 2000 VADM stack (33). (C) PISO 1500 VADM stack (34). (D) ^{10}Be/^{9}Be ratios stack from marine sediments (23). (E) Xifeng loess mean grain size. (F) LR04 benthic δ^{18}O stacks (31), the red and blue areas indicate interglacial and glacial stages respectively. S_1-S_8 indicates the Chinese paleosol layers. The blue numbers on the bottom indicate interglacial marine isotope stages 1-21. The gray bars denote the 13 geomagnetic excursions (I-XIII) and Brunhes/Matuyama (BM) reversal determined by loess ^{10}Be. I-Laschamp; II-Norwegian Greenland Sea; III-Fram Strait; IV-Blake; V-Baffin Bay/6α; VI-Iceland Basin; VII-Pringle Falls; VIII-Portuguese Margin; IX-Levantine; X-Emperor; XI-Big Lost; XII-La Palma/15β; XIII-Stage 17/Osaka Bay.

Figure 3. Comparison of Xifeng loess ^{10}Be reconstructed AM rainfall history with other climate records. (A) The interhemispheric summer solar insolation gradient (June 30°N minus 30°S) (52). (B) Chinese speleothem δ^{18}O (32). (C) High-pass (<23 kyr) filtered results of Chinese speleothem δ^{18}O (black) and ^{10}Be-rainfall (orange). (D) ^{10}Be reconstructed rainfall. (E) LR04 benthic δ^{18}O stack (31).

Figure 4. Spectral results and cross-wavelet transform spectra of Xifeng loess ^{10}Be-derived AM rainfall and geomagnetic field variations. (A) Comparison of ^{10}Be-rainfall (red) and $^{10}Be_{GM}$ flux records (blue). (B) Spectral results of ^{10}Be-rainfall (red) and geomagnetic field (blue) records, black lines indicate the 95% false-alarm level. (C) Cross-wavelet spectrum of ^{10}Be-rainfall and $^{10}Be_{GM}$ flux, black contours indicate the 95% false-alarm level.

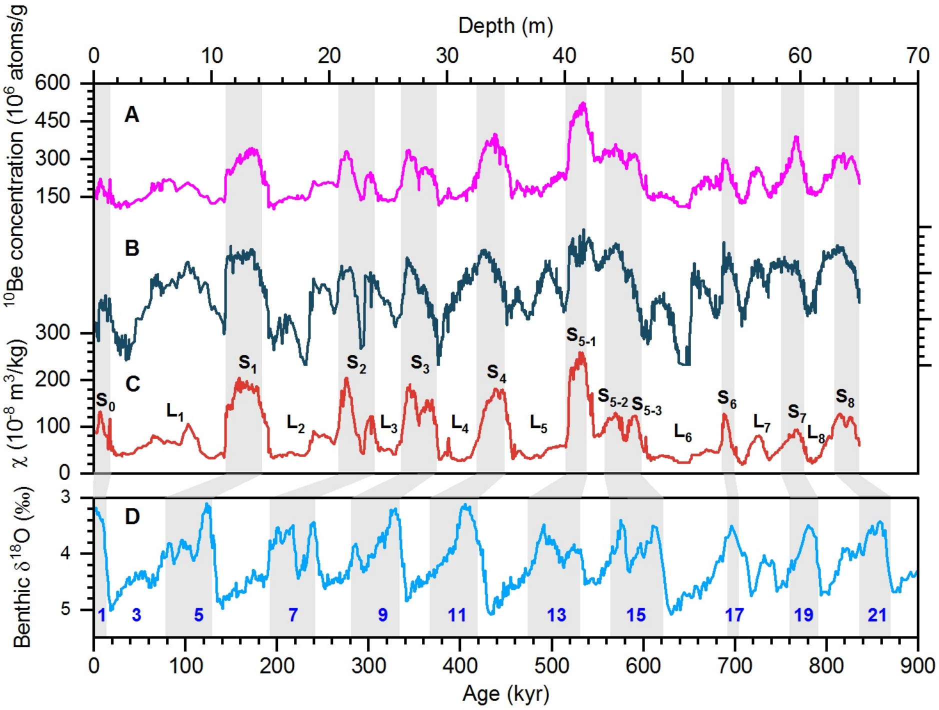

Depth (m)
^{10}Be concentration (10^6 atoms/g)
A
B
C
D
MGS (μm)
χ (10^{-8} m^3/kg)
Benthic δ^{18}O (‰)
Age (kyr)
S$_0$
L$_1$
S$_1$
L$_2$
S$_2$
L$_3$
S$_3$
L$_4$
S$_4$
L$_5$
S$_{5-1}$
S$_{5-2}$
S$_{5-3}$
L$_6$
S$_6$
L$_7$
S$_7$
L$_8$
S$_8$

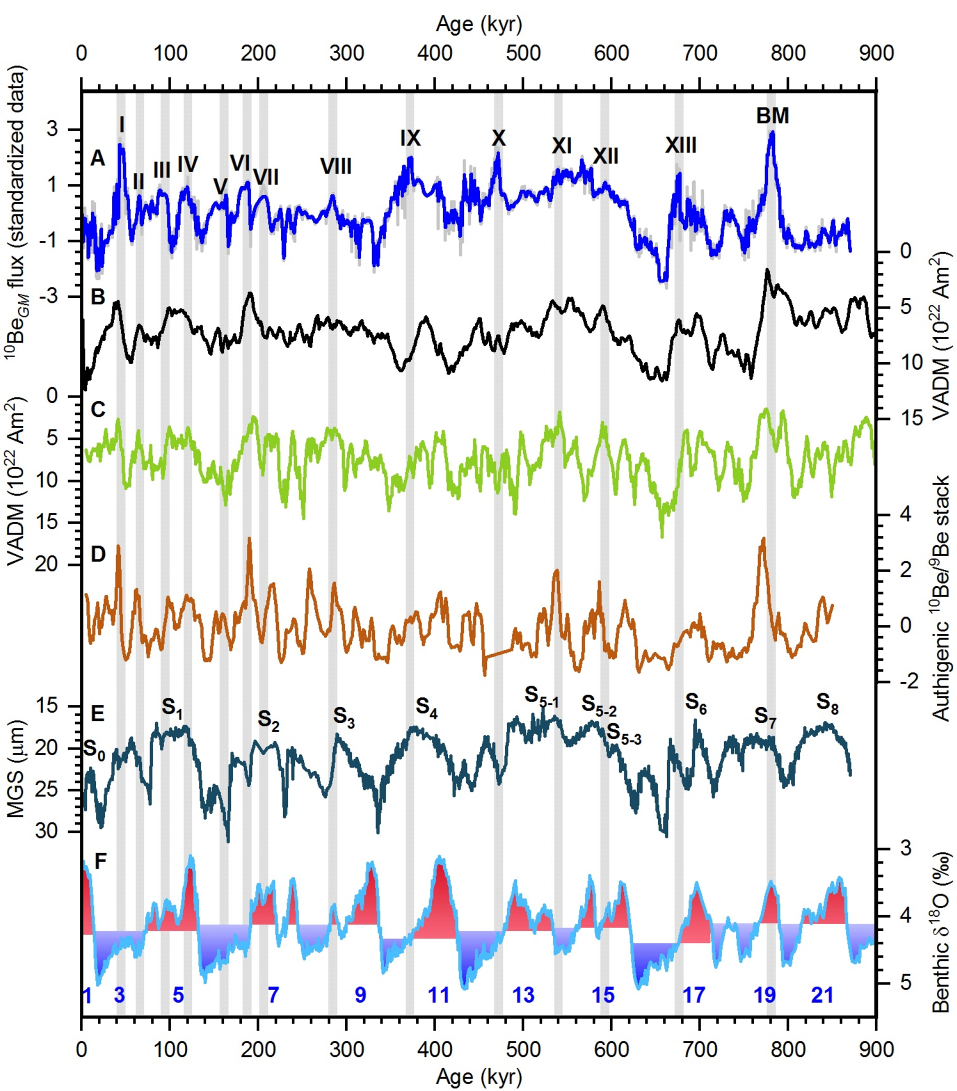

Age (kyr)
$^{10}Be_{GM}$ flux (standardized data)
VADM (10^{22} Am^2)
Authigenic $^{10}Be/^{9}Be$ stack
MGS (μm)
Benthic δ^{18}O (‰)
A
B
C
D
E
F
I
II
III
IV
V
VI
VII
VIII
IX
X
XI
XII
XIII
BM
S_0
S_1
S_2
S_3
S_4
S_{5-1}
S_{5-2}
S_{5-3}
S_6
S_7
S_8
1
3
5
7
9
11
13
15
17
19
21

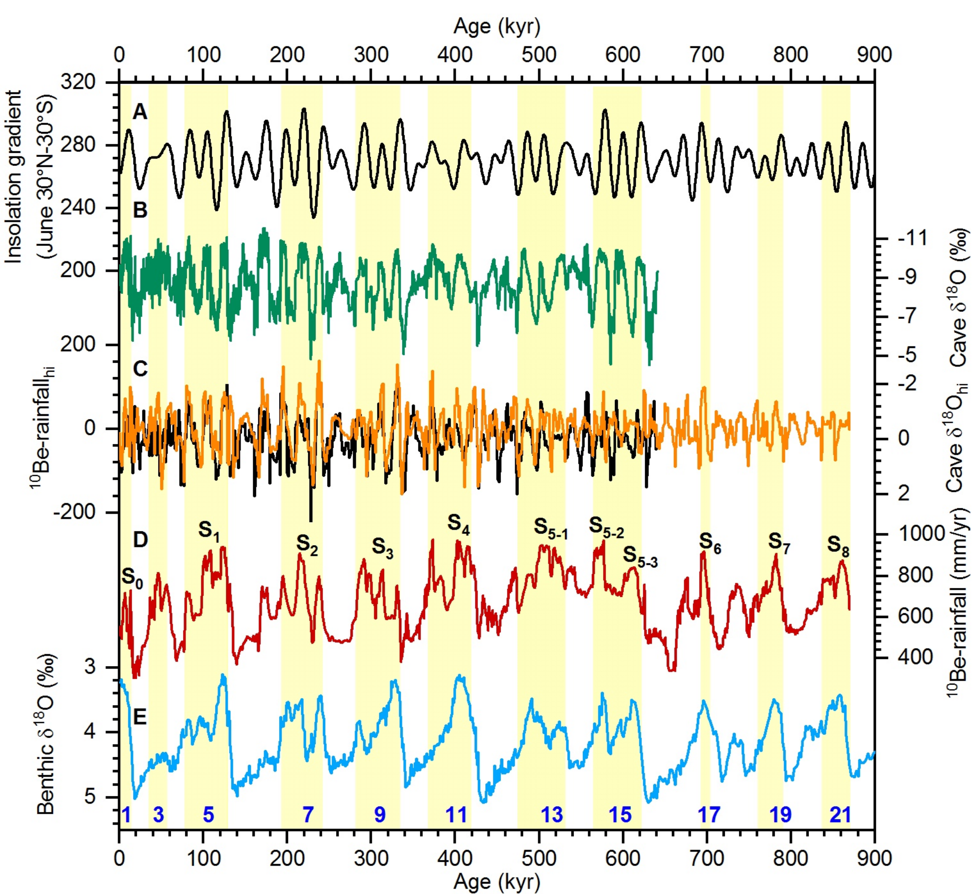

Age (kyr)
Insolation gradient (June 30°N-30°S)
^{10}Be-rainfall$_{hi}$
Cave δ^{18}O (‰)
Cave δ^{18}O$_{hi}$
^{10}Be-rainfall (mm/yr)
Benthic δ^{18}O (‰)
A
B
C
D
E
S$_0$
S$_1$
S$_2$
S$_3$
S$_4$
S$_{5-1}$
S$_{5-2}$
S$_{5-3}$
S$_6$
S$_7$
S$_8$
1
3
5
7
9
11
13
15
17
19
21

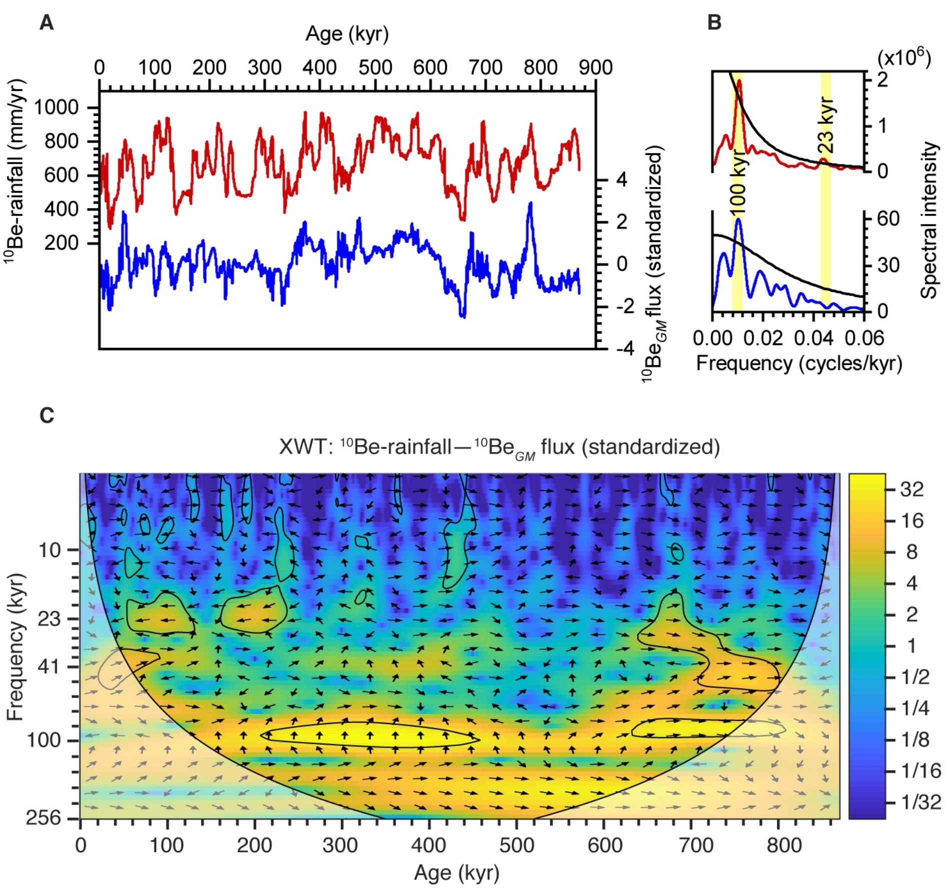
A
Age (kyr)
0 100 200 300 400 500 600 700 800 900
10Be-rainfall (mm/yr)
1000 800 600 400 200
10BeGM flux (standardized)
4 2 0 -2 -4
B
(x10^6)
2 1 0
100 kyr
23 kyr
60 30 0
Spectral intensity
0.00 0.02 0.04 0.06
Frequency (cycles/kyr)
C
XWT: 10Be-rainfall—10BeGM flux (standardized)
Frequency (kyr)
10 23 41 100 256
32 16 8 4 2 1 1/2 1/4 1/8 1/16 1/32
0 100 200 300 400 500 600 700 800
Age (kyr)

Supplementary Information for

Eccentricity-paced geomagnetic field and monsoon rainfall variations over the last 870 kyr

Weijian Zhou, Xianghui Kong, Greig A. Paterson, Youbin Sun, Yubin Wu, Hong Ao, Feng Xian, Yajuan Du, Ling Tang, Jie Zhou, Zhengguo Shi, A. J. Timothy Jull, Guoqing Zhao, Zhisheng An

Correspondence to Zhisheng An (anzs@loess.llqg.ac.cn) and Weijian Zhou (weijian@loess.llqg.ac.cn)

This PDF file includes:

Supplementary Text

Figures S1 to S7

Table S1

SI References

Supplementary Text

Sample collection and measurements. We sampled ~65 m thick loess section covering the strata of S_0-S_8 loess-paleosol sequences at 1 cm interval in field from Xifeng (35.8°N, 107.6°E) in the central Chinese Loess Plateau (Fig. S1). To ensure the continuity of field sampling, different adjacent profiles were excavated (Fig. S1B), and cross-sectional (horizontal) correlation was carried out using a water-tube bubble level. A total of 1302 samples were crushed and homogenized in the lab. The laboratory measurements for ^{10}Be concentration, magnetic susceptibility, grain size and bulk density were conducted at 4 cm intervals for ~83% loess samples, at 2 cm intervals for ~4% samples around B/M reversal and at ~10 cm interval on average for the remaining samples. Magnetic susceptibility was measured using a Bartington MS2 susceptibility meter at 465 Hz. For grain size analysis, all the samples were pretreated by adding 30% hydrogen peroxide (H_2O_2) and 6 N hydrochloric acid (HCl) to remove organic matter and calcium carbonate, and then measured using a Malvern Mastersizer 2000 laser-diffraction analyzer at the State Key Laboratory of Loess and Quaternary Geology, Chinese Academy of Sciences in Xi'an. The ^{10}Be was chemically extracted and purified at the Xi'an Accelerator Mass Spectrometer (AMS) Center, Xi'an (see Materials and Methods), and measured using a 3MV AMS with precision better than 3%. Isotope ratios were normalized to ^{10}Be/^{9}Be ratio of the NIST SRM-4325 standard of 2.68×10^{-11} and corrected by each chemical processing blank. Bulk sample density was derived by dividing the weight of a 2 cm cubic loess sample by its volume obtained by measuring the height, width, and length. Bulk density was used in combination with the loess accumulation rate and decay-corrected ^{10}Be concentrations to calculate the ^{10}Be flux record.

Separating rainfall and geomagnetic signals from loess ^{10}Be. Zhou et al. (2007) indicated that there was a strong similarity between loess susceptibility (χ) and ^{10}Be concentration, which suggested that they were both related to common climate factors (1). For loess ^{10}Be and χ, they both have inherited dust recycled fractions (1). Furthermore, loess χ is well known to be linked to soil moisture content (2, 3), which is correlated with Asian monsoon (AM) rainfall. Similarly, the fallout flux of meteoric ^{10}Be is also known to be linked to rainfall amount, where ^{10}Be is scavenged from the atmosphere by falling raindrops (4, 5). However, there is an additional effect controlling ^{10}Be flux, which is the modulation of ^{10}Be production rate by geomagnetic field variations. Zhou et al. (2007) developed a method to deconvolve the climate and geomagnetic field effects from one another, in order to independently derive records of rainfall and geomagnetic field intensity (1).

We began by correcting the magnetic susceptibility record for inherited fraction from recycled dust using the observed relationship between remnant magnetic coercivity and magnetic susceptibility (6). This revealed a two-component mixing relationship between dry (inherited) and wet (*in-situ* produced) magnetic susceptibility. Based on this relationship we estimated the background value of magnetic susceptibility from recycled dust to be ~25×10^{-8} m^3/kg (1). As shown in Fig. 1 of the main paper, it is at the same level as the low values of magnetic susceptibility during all glacial periods since 870 kyr. This makes sense, since glacial periods are much dryer than interglacials. We use this same value in our current paper.

We next use the observed linear relation between the ^{10}Be concentration and the magnetic susceptibility (Fig. S5A) to derive the inherited dust signal of ^{10}Be. We calculate the recycled dust fraction of ^{10}Be by using this linear-regression correlation and the recycled dust value of magnetic susceptibility (~25×10^{-8} m^3/kg). We estimated this to be ~150×10^6 atoms/g, which is also consistent with the lowest level of ^{10}Be concentration during (very dry) glacial periods (Fig. S5B). We likewise use this value to correct for recycled (inherited) ^{10}Be in the current paper.

We note however, that only ~76% of the covariance in the magnetic susceptibility/^{10}Be data is explained by the observed linear relationship (Fig. S5A). Zhou et al. (2007) asserted that the remaining residual variance was mainly associated with geomagnetic field variations affecting ^{10}Be production rate and hence its meteoric flux (1). This geomagnetic field modulated ^{10}Be fraction is transformed into flux ($^{10}Be_{GM}$ flux) through multiplying by the loess accumulation rate (determined from the age model) and bulk density, and finally a long-term trend is further detrended from it. For further comparison, we calibrate the Xifeng loess $^{10}Be_{GM}$ flux by using absolute virtual axial dipole moment values (VADM) to reconstruct a ^{10}Be-derived VADM record adopting the same method reported in (7) (Fig. S2). We separate our dataset into four intervals: 0-50 kyr including the Laschamp excursion, 50-750 kyr excluding the Laschamp excursion and the Brunhes-Matuyama reversal periods, 750-870 kyr including the Brunhes-Matuyama reversal, and the whole interval 0-870 kyr. For each time interval, average $^{10}Be_{GM}$ flux and absolute VADM values (7) are calculated to discriminate the data in three clusters defined as data lower than mean-1σ, data comprised between mean-1σ and mean+1σ, and data higher than mean+ 1σ limits.

The method of precipitation reconstruction in this study is the same as Beck et al. (2018) (8). We adopt the same formula reported in (8), but modify the intercept according to the modern average precipitation observation record (550 mm/yr) in the Xifeng region. Thus, the equation is given by:

Rainfall (mm/yr)$_{(\text{at time t})}$ = {loess accumulation rate (cm/yr) × bulk density (g/cm^3)× (^{10}Be(M) (atoms/g) - ^{10}Be(D) (atoms/g))/(^{10}Be production rate$_{(\text{at time t})}$/^{10}Be production rate$_{(\text{modern})}$)} × (1.90475 × 10^{-4} (mm × cm^2/atom)) + (501.5 mm/yr)

The ^{10}Be(M) and ^{10}Be(D) indicate measured and dust-recycled ^{10}Be concentration respectively, and the {^{10}Be production rate$_{(\text{at time t})}$/^{10}Be production rate$_{(\text{modern})}$} is calculated from the SINT 2000 record of paleomagnetic field variations (8–10).

Additionally, climatic residual error in the ^{10}Be$_{GM}$ flux and/or uncertainty in ^{10}Be-rainfall is not significant to change our assessment of their orbital-scale variations that we focused on in this study.

Supplementary Figures S1-S7

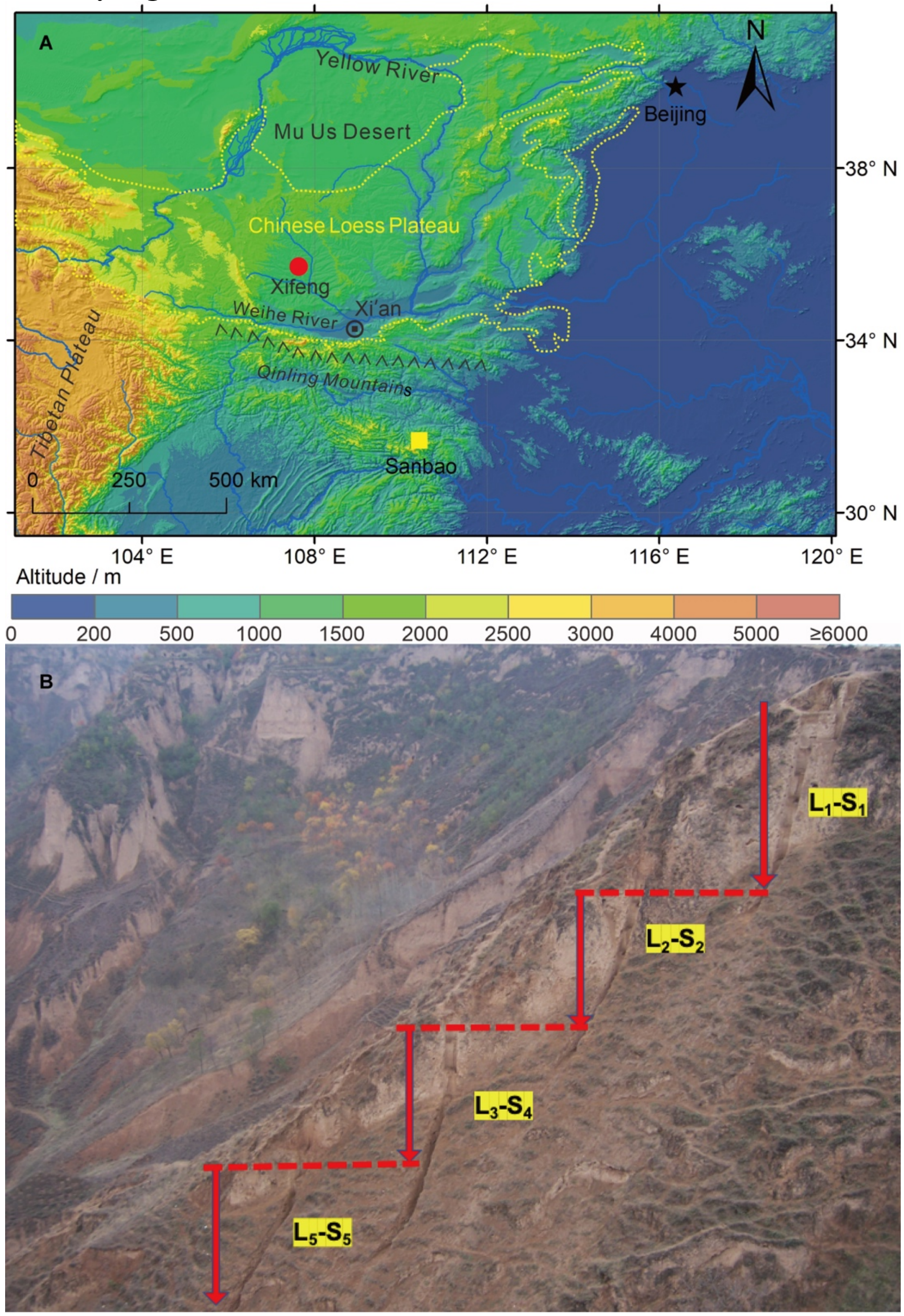

Fig. S1. Location (A) and outcrops (B) of the Xifeng loess on the Chinese Loess Plateau. The red dot and yellow square in A indicate the location of the Xifeng loess profile and Chinese speleothem of Cheng et al. (2016) (11) respectively. Also shown in B are freshly cut sections and strata joints during field sampling. The horizontal dashed lines denote transfer from the bottom of upper sampling profile to the top of lower sampling profile at the same depth level.

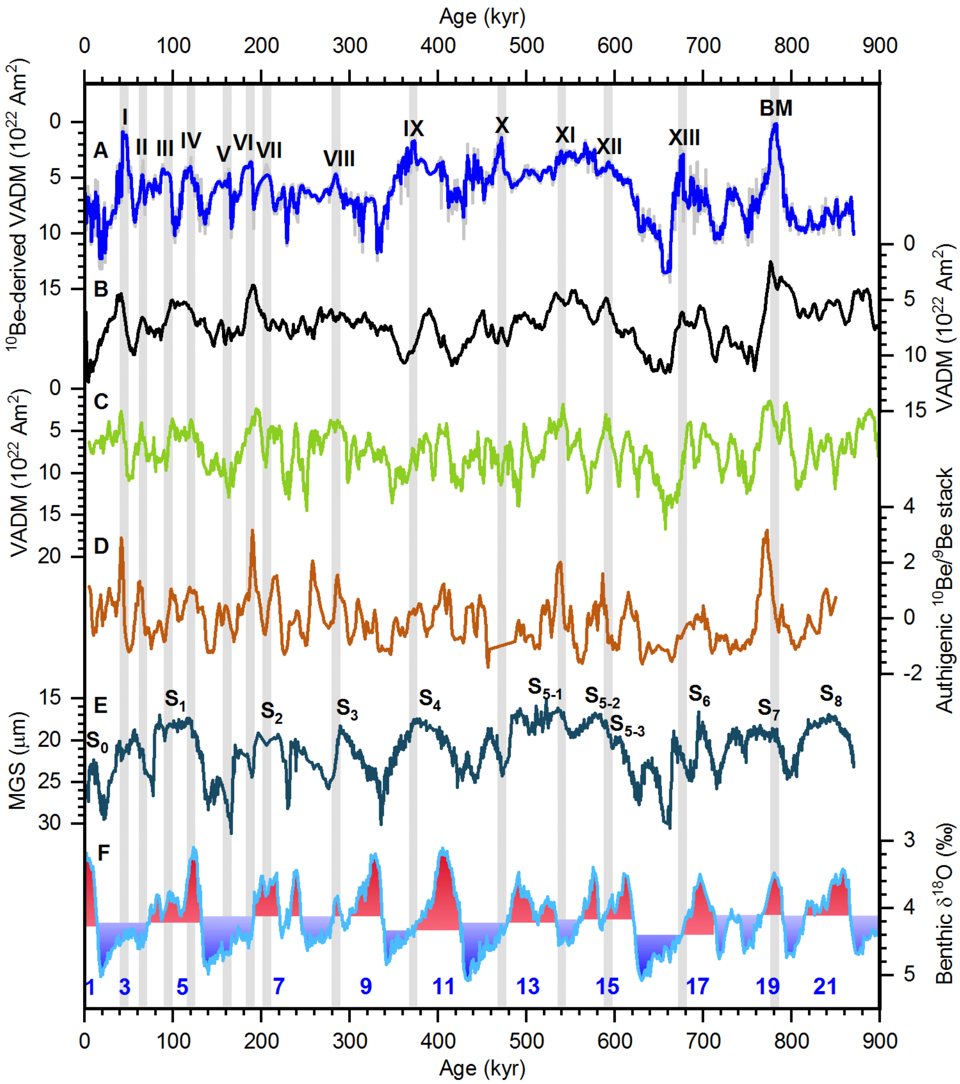

Fig. S2. Comparison of loess ^{10}Be derived paleomagnetic polarity events with other geomagnetic paleointensity records. (A) ^{10}Be-derived VADM from Xifeng loess (gray) and 5 points averaging curve (blue). (B) SINT 2000 VADM stack (10). (C) PISO 1500 VADM stack (12). (D) ^{10}Be/^{9}Be ratios stack from marine sediments (7). (E) Xifeng loess mean grain size. (F) LR04 benthic δ^{18}O stacks (13), the red and blue areas indicate interglacial and glacial stages respectively. S_1-S_8 indicates the Chinese paleosol layers. The blue numbers on the bottom indicate interglacial marine isotope stages 1-21. The gray bars denote the 13 geomagnetic excursions (I-XIII) and Brunhes/Matuyama (BM) reversal determined by loess ^{10}Be. I-Laschamp; II-Norwegian Greenland Sea; III-Fram Strait; IV-Blake; V-Baffin Bay/6α; VI-Iceland Basin; VII-Pringle Falls; VIII-Portuguese Margin; IX-Levantine; X-Emperor; XI-Big Lost; XII-La Palma/15β; XIII-Stage 17/Osaka Bay.

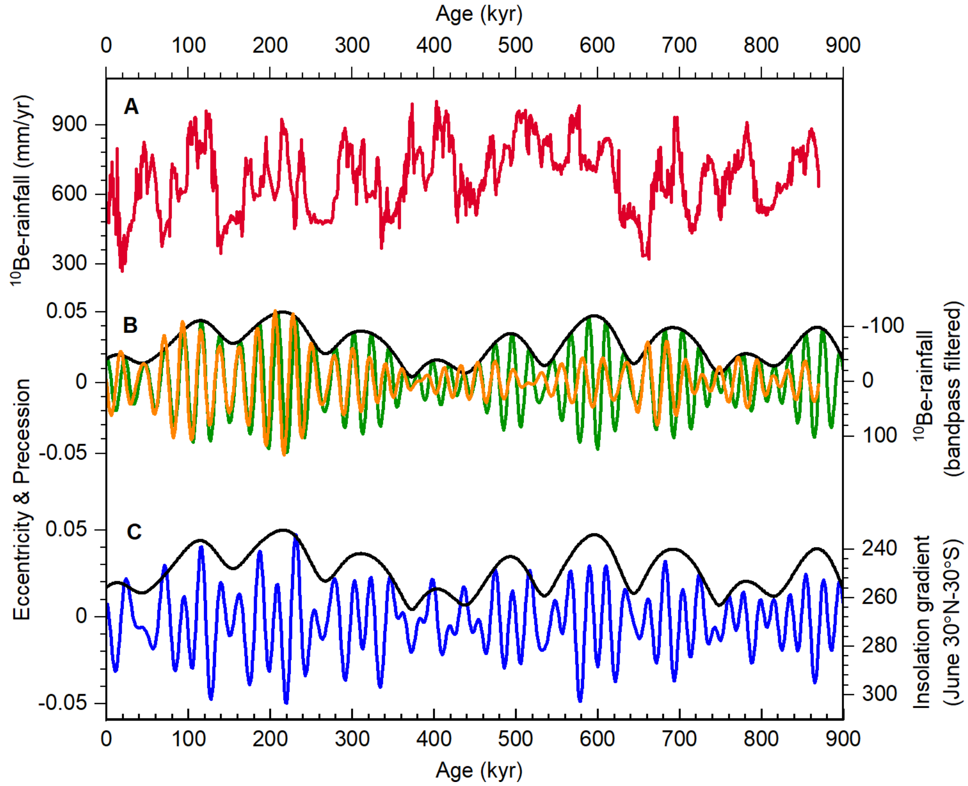

Fig. S3. **Xifeng loess ^{10}Be reconstructed AM rainfall (A), the result after 23 kyr (±20%) bandpass filtering (B, orange) and 30°N to 30°S June solar insolation gradient (C, blue) compared with orbital precession (B, green) and eccentricity** (14) **(B & C, black) parameters.**

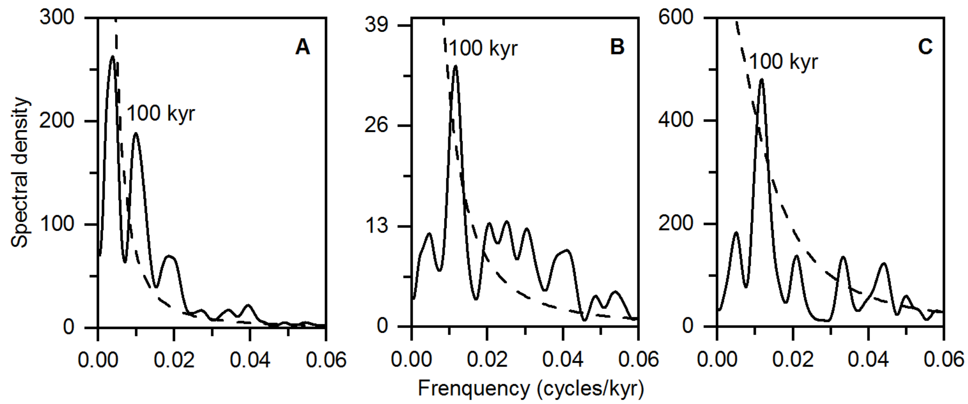

Fig. S4. The spectral results of (A) SINT 2000 (10)**, (B) marine sediment $^{10}Be/^{9}Be$ ratio stack** (7) **and (C) PISO 1500** (12)**.** Dashed lines indicate the 95% false-alarm level. The ~100 kyr cycle is predominant in these records.

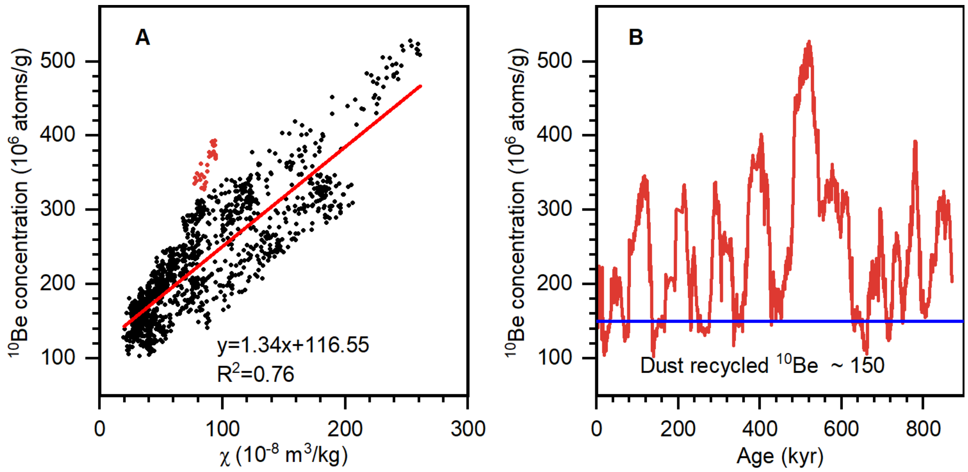

Fig. S5. Determination of recycled dust ^{10}Be concentration. (A) Linear relationship between the ^{10}Be concentration and magnetic susceptibility (χ) after removing a few deviated data (red points) during the B/M reversal interval with minimum geomagnetic field intensity. (B) The ^{10}Be concentration record (red) of Xifeng section and the recycled dust ^{10}Be concentration (blue line).

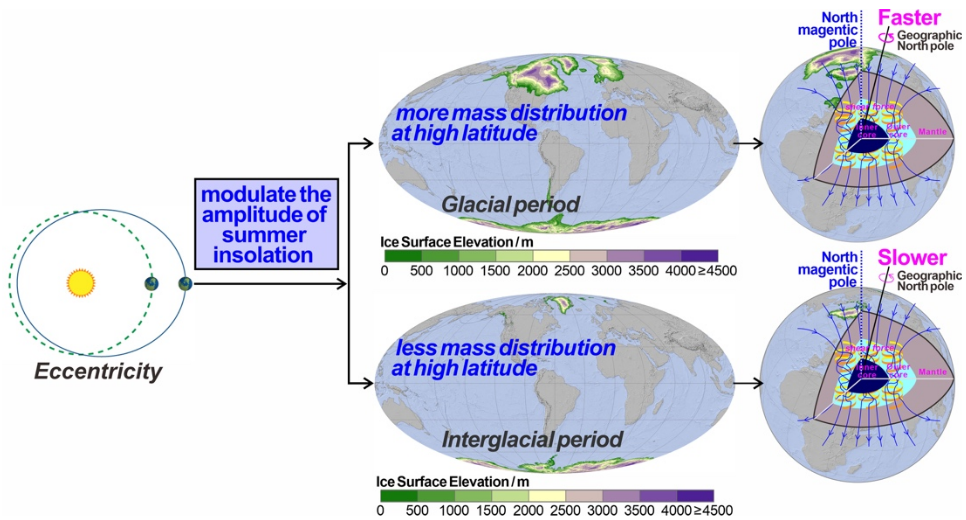

Fig. S6. Illustration showing an influence of eccentricity modulated glacial-interglacial cycles on perturbation of Earth's core and thus the geomagnetic field changes. The thick (thin) arrow circle around the Earth's axis indicates faster (slower) Earth's rotation rate.

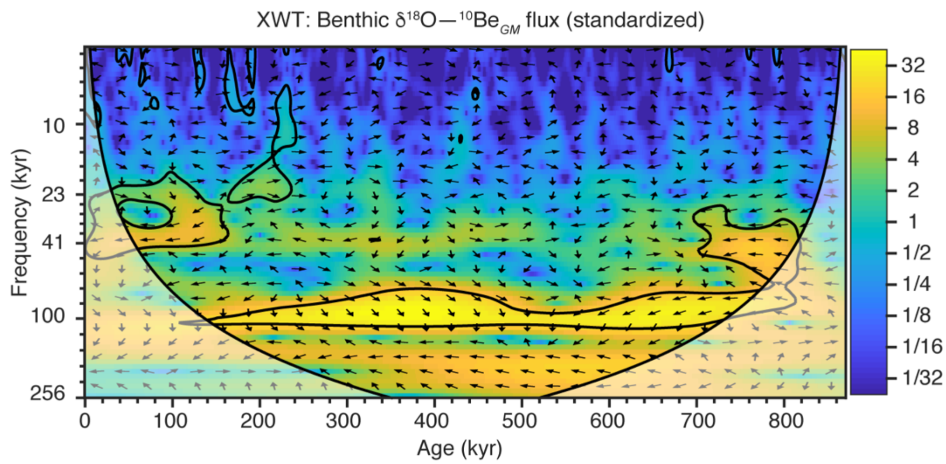

Fig. S7. The cross-wavelet result of benthic $\delta^{18}O$ (13) and Xifeng loess $^{10}Be_{GM}$ flux (standardized data).

Supplementary Table

Table S1. Age control points for Xifeng loess chronology*

Numbers	Depth (cm)	Age (kyr)	Note
1	1	0.11	SCP
2	52	5.8	SCP
3	116	11.8	SCP
4	140	14	FCP, MIS1/2
5	276	22	SCP
6	420	31	SCP
7	592	43	SCP
8	1020	69	SCP
9	1116	78	FCP, MIS4/5
10	1168	86	SCP
11	1204	98	SCP
12	1300	110	SCP
13	1356	120	SCP
14	1428	129	FCP, MIS5/6
15	1775	164	SCP
16	1965	177	SCP
17	2015	187	SCP
18	2075	192	FCP, MIS6/7
19	2105	196	SCP
20	2125	210	SCP
21	2225	225.4	SCP
22	2305	233	SCP
23	2385	242	FCP, MIS7/8
24	2551	273.8	SCP
25	2607	281	FCP, MIS8/9
26	2695	294	SCP
27	2735	301	SCP
28	2783	309	SCP
29	2831	315	SCP
30	2871	329	SCP
31	2911	334	FCP, MIS9/10
32	3251	367	FCP, MIS10/11
33	3307	374	SCP
34	3359	387	SCP

35	3383	398	SCP
36	3491	419	FCP, MIS11/12
37	3543	427	SCP
38	3887	462	SCP
39	4007	474	FCP, MIS12/13
40	4071	494	SCP
41	4135	513	SCP
42	4187	531	FCP, MIS13/14
43	4339	564	FCP, MIS14/15
44	4435	578	SCP
45	4655	622	FCP, MIS15/16
46	5071	664	FCP
47	5231	678	FCP
48	5331	692	FCP, MIS16/17
49	5439	704	FCP, MIS17/18
50	5559	724	FCP
51	5687	744	FCP
52	5839	760	FCP, MIS18/19
53	6035	791	FCP, MIS19/20
54	6287	836	FCP, MIS20/21
55	6375	852	FCP
56	6499	870	FCP, MIS21/22

*Because both the Chinese loess-paleosol sequence (15, 16) and speleothem $\delta^{18}O$ sequence (11, 17) record the Asian monsoon variation with the same precession cycle, we use speleothem $\delta^{18}O$ record with high-precision U/Th dated ages to refine the time scale of Xifeng loess based on common features observed in the Xifeng ^{10}Be-based rainfall record and the absolute U/Th dated Chinese speleothem $\delta^{18}O$ variations.

FCP: First-order age control points by correlating rapid changes in Xifeng loess grain size with the glacial/interglacial transitions in the marine isotope records (13). **SCP**: Second-order age control points based on common features observed in the rainfall-related ^{10}Be flux and the U/Th dated Chinese speleothem $\delta^{18}O$ variations (11). **MIS**: Marine isotope stage. The average age resolution of Xifeng section is ~0.7 kyr.

SI References

1. W. Zhou, *et al.*, Disentangling geomagnetic and precipitation signals in an 80-kyr Chinese loess record of ^{10}Be. *Radiocarbon* **49**, 139–160 (2007).
2. Z. An, G. J. Kukla, S. C. Porter, J. Xiao, Magnetic susceptibility evidence of monsoon variation on the Loess Plateau of central China during the last 130,000 years. *Quat. Res.* **36**, 29–36 (1991).
3. B. A. Maher, Palaeoclimatic records of the loess/palaeosol sequences of the Chinese Loess Plateau. *Quat. Sci. Rev.* **154**, 23–84 (2016).
4. Y. Ishikawa, H. Murakami, T. Sekine, K. Yoshihara, Precipitation scavenging studies of radionuclides in air using cosmogenic ^{7}Be. *J. Environ. Radioact.* **26**, 19–36 (1995).
5. A. M. Smith, et al., ^{7}Be and ^{10}Be concentrations in recent firn and ice at Law Dome, Antarctica. *Nucl. Instruments Methods Phys. Res. Sect. B Beam Interact. with Mater. Atoms* **172**, 847–855 (2000).
6. M. E. Evans, F. Heller, Magnetism of loess/palaeosol sequence: Recent developments. *Earth-Science Rev.* **54**, 129–144 (2001).
7. Q. Simon, *et al.*, Authigenic ^{10}Be/^{9}Be ratio signatures of the cosmogenic nuclide production linked to geomagnetic dipole moment variation since the Brunhes/Matuyama boundary. *J. Geophys. Res. Solid Earth* **121**, 7716–7741 (2016).
8. J. W. Beck, *et al.*, A 550,000-year record of East Asian monsoon rainfall from ^{10}Be in loess. *Science.* **360**, 877–881 (2018).
9. G. Wagner, *et al.*, Reconstruction of the geomagnetic field between 20 and 60 kyr BP from cosmogenic radionuclides in the GRIP ice core. *Nucl. Instruments Methods Phys. Res. Sect. B Beam Interact. with Mater. Atoms* **172**, 597–604 (2000).

10. J. P. Valet, L. Meynadier, Y. Guyodo, Geomagnetic dipole strength and reversal rate over the past two million years. *Nature* **435**, 802–805 (2005).

11. H. Cheng, *et al.*, The Asian monsoon over the past 640,000 years and ice age terminations. *Nature* **534**, 640–646 (2016).

12. J. E. T. Channell, C. Xuan, D. A. Hodell, Stacking paleointensity and oxygen isotope data for the last 1.5 Myr (PISO-1500). *Earth Planet. Sci. Lett.* **283**, 14–23 (2009).

13. L. E. Lisiecki, M. E. Raymo, A Pliocene-Pleistocene stack of 57 globally distributed benthic $\delta^{18}O$ records. *Paleoceanography* **20**, 1–17 (2005).

14. A. Berger, M. Loutre, Insolation values for the climate of the last 10 million years. *Quat. Sci. Rev.* **10**, 297–317 (1991).

15. Z. Guo, et al., Summer monsoon variations over the last 1.2 Ma from the weathering of loess‐soil sequences in China. *Geophys. Res. Lett.* **27**, 1751‐1754 (2000).

16. Y. Sun, et al., Astronomical and glacial forcing of East Asian summer monsoon variability. *Quat. Sci. Rev.* **115**, 132–142 (2015).

17. Y. Wang, et al., Millennial- and orbital-scale changes in the East Asian monsoon over the past 224,000 years. *Nature* **451**, 1090–1093 (2008).